SUPLEMENTARY MATERAL
Control of vortex chirality in symmetric ferromagnetic rings using ferromagnetic nanoelement

Uladzislau Makartsou,* Mathieu Moalic, Mateusz Zelent, and Maciej Krawczyk[†]

Institute of Spintronics and Quantum Information,
Faculty of Physics, Adam Mickiewicz University,
Uniwersytetu Poznańskiego 2, 61-614 Poznań, Poland

Michal Mruczkiewicz

Institute of Electrical Engineering, Slovak Academy of Sciences, Dubravska cesta 9,
SK-841-04 Bratislava, Slovakia and Centre For Advanced Materials Application CEMEA,
Slovak Academy of Sciences, Dubravska cesta 9, 845 11 Bratislava, Slovakia
(Dated: July 30, 2023)

1. Statistic approach

In this section, we discuss the estimation of the statistical error of the chirality control achieved in micromagnetic simulations by the pseudo-random distribution of grains correlated with the distribution of the magnetization. Initial simulations of nanoring (NR) without nanoelement (NE) demagnetization to remanence, performed without grains, and repeated 100 times with exactly the same input code of micromagnetic solver, showed that a clockwise (CW) configuration was obtained for 97% of the cases [see Fig. S1 (a)]. This testifies to the nondeterministic character of micromagnetic simulations, resulting from numerical noise. This results also in the dominance of NR relaxation to
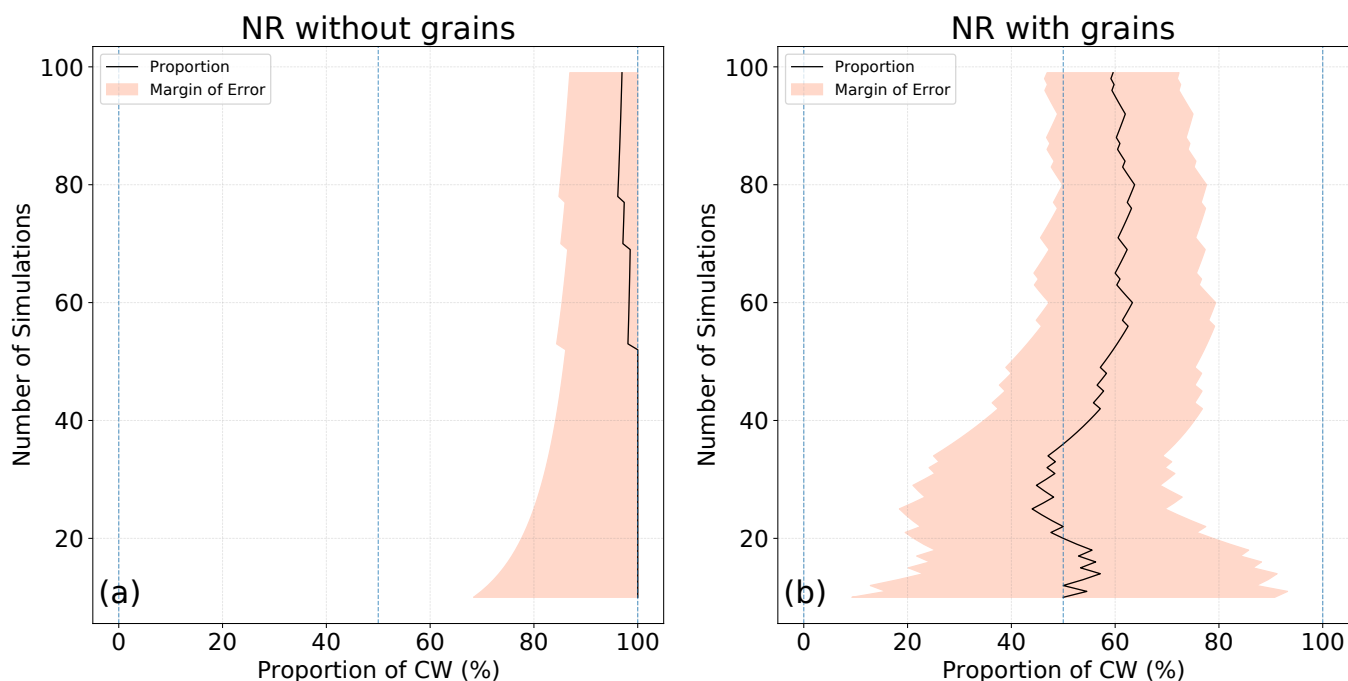

FIG. S1. (a) The dependence of the proportion of CW cases obtained for NR without grains with marked a margin of error (MOE) on a number of simulations (MOE was calculated according to Eq. S2). (b) The probability of CW chirality with MOE for NR with grains, where MOE was calculated according to Eq. S1.

_____

* ulamak@st.amu.edu.pl
[†] krawczyk@amu.edu.pl

one selected chirality, despite the full symmetry of the system. To obtain randomness, we introduced a pseudorandom number, which determines the spatial semi-random distribution of magnetization of the NR in the form of grains. As shown in Fig. S1(b), for 100 simulations we receive a proportion of 60% CW and 40% CCW vortex state chirality in remanence. However, the pseudo-random nature of the grain distribution shouldn't express the predominance of CW over CCW vortex chirality. Thus, to estimate the statistical error in our numerical results we introduce a margin of error (MOE) according to Eq. S1, with a confidence interval of 99% (we assumed that value to cover the expected probability 50% for CW or CCW configurations in performed simulations), which correspond to z-score equal 2.576 [S1]:

$$\text{MOE} = 2.576 \times \sqrt{\frac{\hat{p}(1-\hat{p})}{n}}. \tag{S1}$$

The term $\hat{p}$ refers to the proportion of successes with the number n of simulations. We can use formula S1 only if the following requirements are met: $n\hat{p} \leq 5$ and $n(1-\hat{p}) \leq 5$ [S1]. For cases that did not meet these requirements [for all simulations without NE, and with NE between 0 and 400 for parallel and anit-parallel NE configuration, see Fig. S2 (a-c)], the MOE depends only on the number of simulations:

$$\text{MOE} = \frac{0.98}{\sqrt{n}}. \tag{S2}$$

For simulations that present dominant CCW or CW chirality with the presence of parallel and anti-parallel NE configurations, respectively, we used MOE with a confidence interval of 95%.
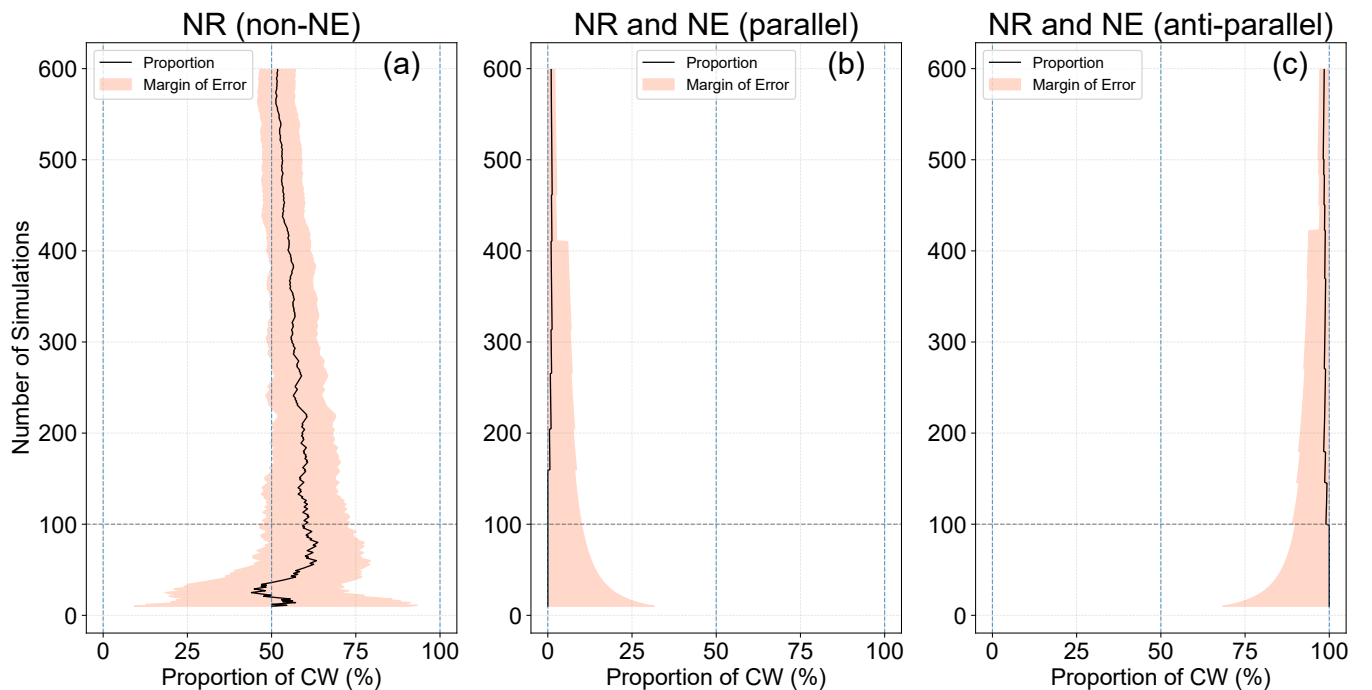

FIG. S2. (a) Extended up to 600 simulations a probability of CW chirality state in remanence in dependence on n with MOR calculated according to Eq. S1 for NR with grains. (b),(c) Proportion of CW state in remanence for 600 simulations for parallel and anti-parallel configurations of NE inside the NR with grains. MOE is calculate from Eq. S2 for $n < 400$ simulations and with Eq. S1 for $n \geq 400$ simulations.

To demonstrate the equal probability of CW and CCW chirality after relaxation for NR at remanence we increased the number of simulations to 600 (see Fig. S2(a) and Fig. 2 in the main text). The proportion of CW and CCW states tends to 50%. For NR with NE system with a parallel configuration, we found 1% of simulations with CW chirality after 600 simulations [see Fig. S2(b)]. For the anti-parallel configuration, we observed CW chirality in 98.5% cases, Fig. S2(c)). We attribute this slight deviation from 100% by specific pseudo-random grain and magnetization distribution, which at one selected case strongly determines the chirality of the nanoring's magnetization.

The hysteresis loop in Fig. S3 shows the relationship between magnetization and the applied magnetic field along the y-axis in the full considered range, i.e., from -2000 mT to 2000 mT for the NR without NE. It exhibits a characteristic shape with two distinct switching fields due to the ring geometry.
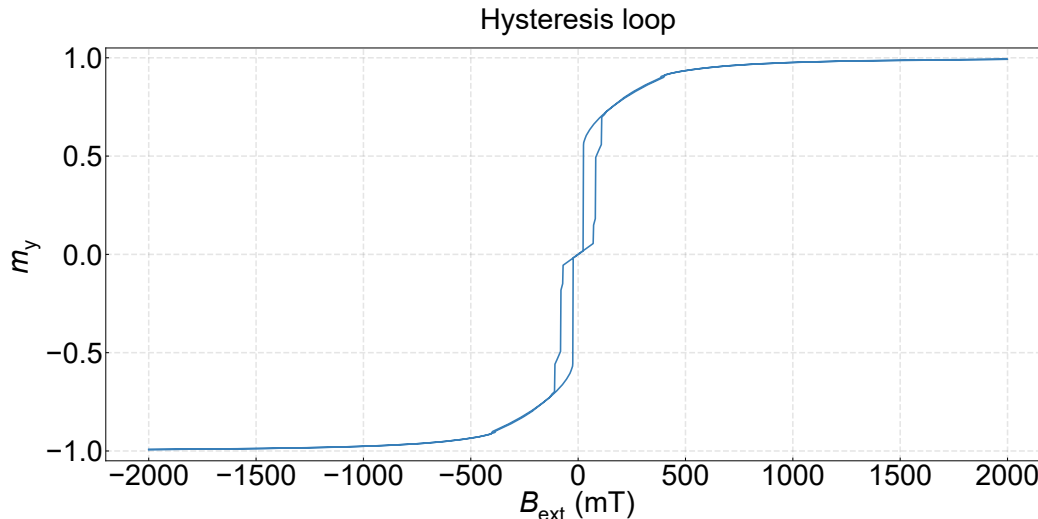

FIG. S3. Hysteresis loop in the magnetic field values from -2000 mT to 2000 mT.

3. *Magnetization*

Animation 1 (see file anim-sup-1.mp4) with the screenshot shown in Fig. S4) illustrates the evolution of the magnetization in NR for the four configurations described in Fig. 5 of the main text.

This animation visualizes the change in magnetization as the field decreases during the remagnetization process. We obtained the animation by performing two independent simulations for each configuration. (i) Starting at 100 mT and presenting the evolution of magnetization along the hysteresis loop with a step of 1 mT. (ii) To precisely visualize the transition from the onion state (OS) to the vortex state (VS) at the switching field, we conducted an additional simulation with a time step of 0.1 nanoseconds. After demagnetization, we obtained a VS with a chirality that depends on the magnetization orientation of the NE for cases (a) and (b) and on the grain distribution for cases (c) and (d) in Fig. S4.

4. *Effective magnetic field*

Figure S5 illustrates the azimuthal component of the effective magnetic field $B_{\varphi,\text{eff}}$ divided into two parts (left and right) with flipped signs to ensure symmetry with respect to the y-axis. This visualization reveals the relationship between the orientation of the external magnetic field and the magnetization texture of NR and NE. The direction of evolution of the magnetization texture is determined by the movement of domain walls, which is caused by the difference in the effective field intensity on the sides of the NR. It is shown in Fig. S5 as the averaged effective field on both sides of the vertically divided NR. Here the averaged intensities of the effective field were calculated inside the left and right parts of the NR.

In Fig. S5 (a) and (c), i.e., in the case of an anti-parallel alignment of the magnetization in NR and NE, and non-NE configuration with different distribution of M_S in the grains resulting in CW chirality, the right part has a smaller absolute average magnitude of the $B_{\varphi,\text{eff}}$ than the left part, leading the domain walls (DWs) movement to the right side.

Conversely, in Fig. S5(b) and (d), with a parallel alignment of the magnetization in NR and NE, and a non-NE configuration with the same random distribution of M_S in the grains, the left part has a smaller absolute average
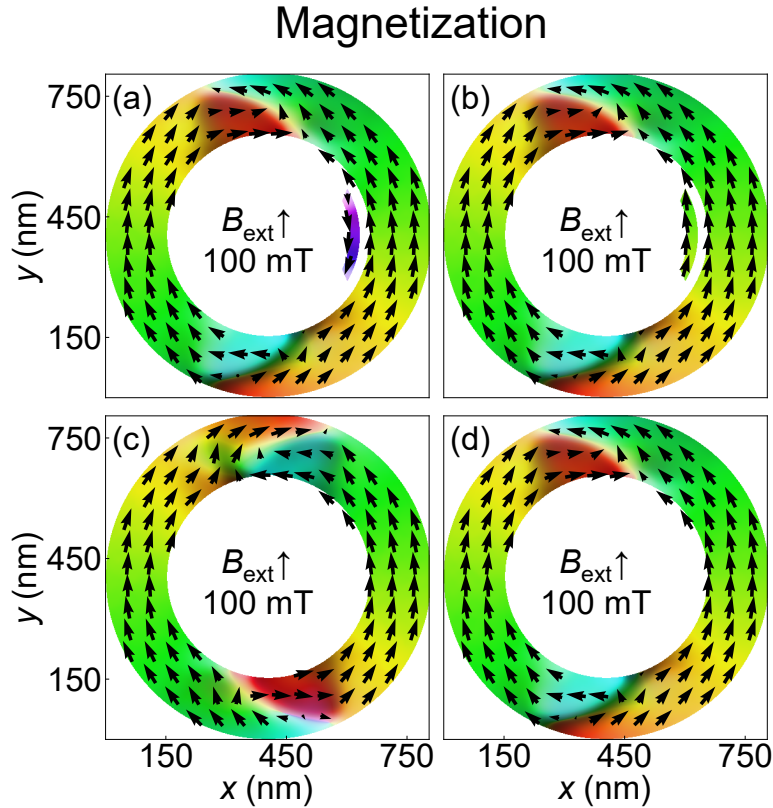
Magnetization

FIG. S4. The initial snapshots of the magnetization evolution animation for four considered scenarios at external magnetic field 100 mT. (a) Anti-parallel configuration, (b) parallel configuration, (c) and (d) – non-NE configurations with two different random distributions of M_{S} in the grains.

magnitude of $B_{\varphi,\mathrm{eff}}$, leading DWs movement to the left side relative to the magnetic field, and CCW.

5. Torque evolution

Figure S6 shows a snapshot of an animation (see the file anim-sup-2.mp4) that illustrates the average azimuthal component of the torque $\overline{\tau}_{\varphi}$ as a function of the external magnetic field B_{ext} and the cross-section of the azimuthal component of the torque texture inside the NR. This visualization reveals the relationship between the amplitude of the external magnetic field and the total torque $\overline{\tau}_{\varphi}$ in the NR. The sign of the total torque $\overline{\tau}_{\varphi}$ predicts the chirality in remanence, which is caused by the difference in the effective field intensity on the sides of the NR, as shown in Fig. S5 and Fig. S6. The torque is determined by Eq. S3 [S2]:

$$\boldsymbol{\tau} = \frac{\gamma_{\mathrm{LL}}}{2} \left[\boldsymbol{m} \times \boldsymbol{B}_{\mathrm{eff}} + \boldsymbol{m}(\boldsymbol{m} \times \boldsymbol{B}_{\mathrm{eff}}) \right]. \tag{S3}$$

[S1] J. O. Bennett and W. L. Briggs, *Using and understanding mathematics : a quantitative reasoning approach* (Addison Wesley) p. 789.

[S2] A. Vansteenkiste, J. Leliaert, M. Dvornik, M. Helsen, F. Garcia-Sanchez, and B. V. Waeyenberge, The design and verification of mumax3, AIP Advances **4**, 107133 (2014).
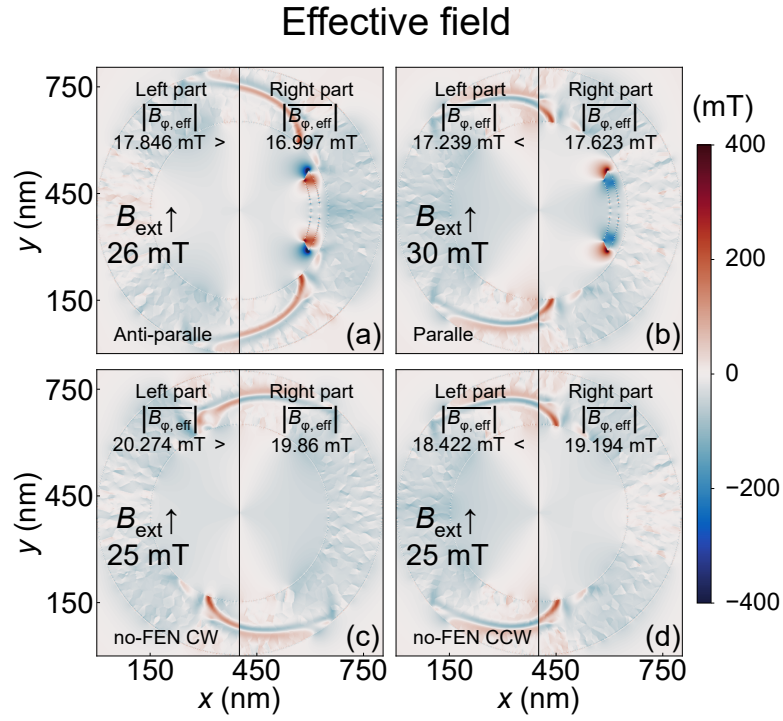
Effective field

FIG. S5. The effective magnetic field of the system just before switching from an OS to VS. (a) Anti-parallel configuration, (b) parallel configuration, ending with CW and CCW VS chiralities, respectively; (c) and (d) – non-NE configuration with random distribution of M_S in the grains resulting in CW and CCW chiralities, respectively.
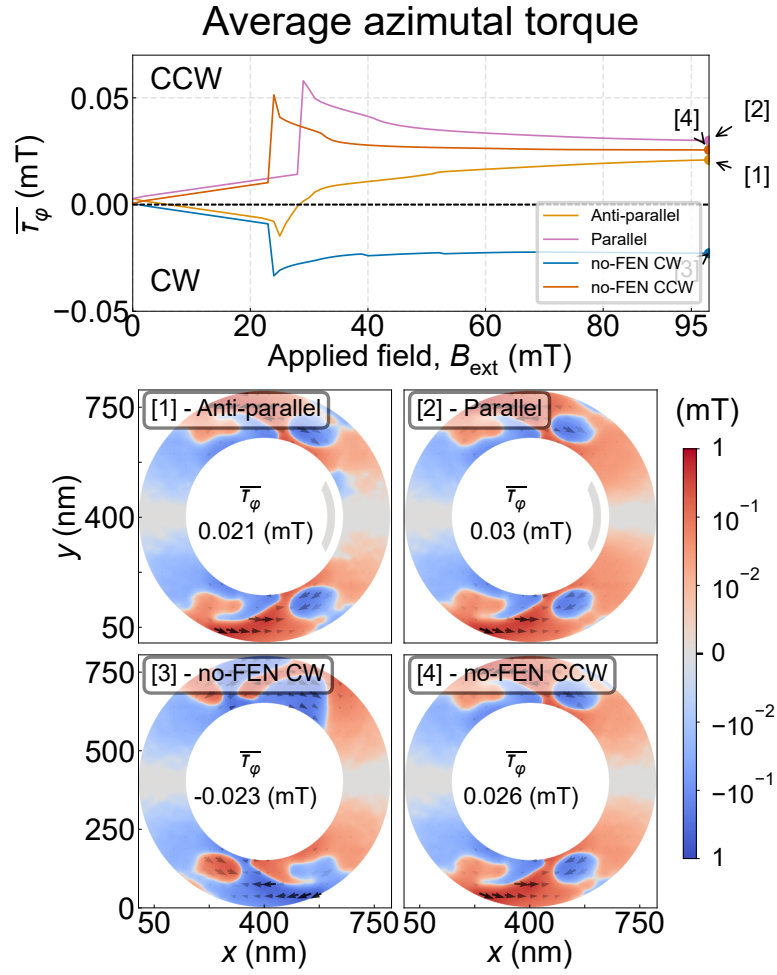
FIG. S6. The azimuthal component of the magnetic torque of the system in field 97 mT. [1] - Anti-parallel, [2] - Parallel, ending with CW and CCW VS chiralities, respectively; [3] - no-FEN CW, and [4] - no-FEN CCW - non-NE configuration with random distribution of M_S in the grains resulting in CW and CCW chiralities, respectively.